ToF Performance Evaluation of PET Modules With Digital Silicon Photomultiplier Technology During MR Operation

David Schug, Jakob Wehner, Peter Michael Dueppenbecker, Bjoern Weissler, Pierre Gebhardt,
Benjamin Goldschmidt, Torsten Solf, Fabian Kiessling, and Volkmar Schulz

Abstract—In 2012, we presented the Hyperion-II$^{\mathrm{D}}$ preclinical PET insert which uses Philips Digital Photon Counting's digital SiPMs and is designed to be operated in a 3-T MRI. In this work we use the same platform equipped with scintillators having dimensions closer to a clinical application. This allows an investigation of the time of flight (ToF) performance of the platform and its behavior during simultaneous MR operation. We employ LYSO crystal arrays of $4 \times 4 \times 10 \ \mathrm{mm}^3$ coupled to 4×4 PDPC DPC 3200-22 sensors (DPC) resulting in a one-to-one coupling of crystals to read-out channels. Six sensor stacks are mounted onto a singles processing unit in a 2×3 arrangement. Two modules are mounted horizontally facing each other on a gantry with a crystal-to-crystal spacing of 217.6 mm (gantry position). A second arrangement places the modules at the maximum distance of approximately 410 mm inside the MR bore (maximum distance position) which brings each module close to the gradient system. The DPCs are cooled down to approximately $5 - 10°\mathrm{C}$ under operation. We disable 20% of the worst cells and use an overvoltage of $V_{\mathrm{ov}} = 2.0$ V and 2.5 V. To obtain the best time stamps, we use the trigger scheme 1 (first photon trigger), a narrow energy window of 511 ± 50 keV and a minimum required light fraction of the main pixel of more than 65% to reject intercrystal scatter. By using a ^{22}Na point source in the isocenter of the modules, the coincidence resolution time (CRT) of the two modules is evaluated inside the MRI system without MR activity and while using highly demanding gradient sequences. Inside the B_0 field without any MR activity at an overvoltage of $V_{\mathrm{ov}} = 2.0$ V, the energy resolution is 11.45% (FWHM) and the CRT is 250 ps (FWHM). At an overvoltage of $V_{\mathrm{ov}} = 2.5$ V, the energy resolution is 11.15% (FWHM) and the CRT is 240 ps (FWHM). During a heavy z-gradient sequence (EPI factor: 49, gradient strength: 30 mT/m, slew rate: 192.3 mT/m/ms, TE/TR: 12/25 ms and switching duty cycle: 67%) at the gantry position and an overvoltage of $V_{\mathrm{ov}} = 2.0$ V, the energy resolution is degraded relatively by 4.1% and the CRT by 25%. Using the same sequence but at the maximum distance position and an overvoltage of $V_{\mathrm{ov}} = 2.5$ V, we measure a degradation of the energy resolution of 9.2% and a 52% degradation of the CRT. The Hyperion-II$^{\mathrm{D}}$ platform proofs to deliver good timing performance and energy resolution inside the MRI system even under highly demanding gradient sequences.

Index Terms—Coincidence techniques, digital integrated circuits, digital signal processing, magnetic resonance imaging, medical imaging, PET, PET instrumentation, scintillation detectors, silicon radiation detectors, semiconductor devices, time resolution, time-of-flight PET.

D. Schug, J. Wehner, and B. Goldschmidt are with the Department of Physics of Molecular Imaging Systems, Institute for Experimental Molecular Imaging, RWTH Aachen University, 52074 Aachen, Germany.

P. M. Dueppenbecker is with the Department of Physics of Molecular Imaging Systems, Institute for Experimental Molecular Imaging, RWTH Aachen University, 52074 Aachen, Germany, and also with the Division of Imaging Sciences and Biomedical Engineering, King's College London, London WC2R 2LS, U.K.

B. Weissler is with the Department of Physics of Molecular Imaging Systems, Institute for Experimental Molecular Imaging, RWTH Aachen University, 52074 Aachen, Germany, and also with the Department of Clinical Application Research, Philips Research, 52066 Aachen, Germany.

P. Gebhardt is with the Division of Imaging Sciences and Biomedical Engineering, King's College London, London WC2R 2LS, U.K.

T. Solf is with Department of Oncology Solutions, Philips Research, 5656 AE Eindhoven, Netherlands.

F. Kiessling is with the Institute for Experimental Molecular Imaging, RWTH Aachen University, 52062 Aachen, Germany.

V. Schulz is with the Department of Physics of Molecular Imaging Systems, Institute for Experimental Molecular Imaging, RWTH Aachen University, 52074 Aachen, Germany, and also with the Department of Clinical Application Research, Philips Research, 52066 Aachen, Germany

Color versions of one or more of the figures in this paper are available online at http://ieeexplore.ieee.org.

Digital Object Identifier 10.1109/TNS.2015.2396295

I. Introduction

POSITRON EMISSION TOMOGRAPHY (PET) offers a high sensitivity for imaging of metabolic processes. For anatomical co-registration, PET is combined with other imaging modalities. PET has been successfully integrated with X-ray computed tomography (CT) [1]. Another combination currently being investigated is the integration of PET and magnetic resonance imaging (MRI or shorter: MR) [2], [3]. PET/MR offers a higher soft tissue contrast and reduces the dose a patient is exposed to in contrast to PET/CT [4]–[7].

The standard light detectors for PET systems were photomultipliers which can not be operated inside strong magnetic fields. Therefore, first PET/MR systems used optical fibers to transport the scintillation light from the gamma detectors located inside the MR bore out of the magnetic field where it is detected by photomultipliers [8]–[10]. By contrast, solid state photo detectors like avalanche photo diodes (APD) allow the operation of the light detector inside magnetic fields. The first systems employing APDs transported the analog signal out of the magnetic field to digitization electronics [11]–[14]. However, APDs offer

no time of flight (ToF) advantage. An overview of PET/MR integrations can be found in [15]–[17].

Analog silicon photomultiplier (SiPM) are made up of an array of highly sensitive single photon avalanche diodes (SPAD). A single SPAD is essentially an APD operated in Geiger-mode giving an analog avalanche signal for each breakdown. All SPADs are coupled together and the sum of the current signal is proportional to the number of SPADs that brake down. SiPMs are suitable for operation in high magnetic fields [18]. First SiPM-based systems transported the analog signals out of the MR bore with no further processing inside the magnetic field [19]–[21]. Other concepts included some analog signal processing within the PET module operated inside the MRI system [22]. Our group employed analog SiPMs and incorporated the complete digitization into an MR-compatible PET module (Hyperion-I) [23], [24].

The same PET module architecture was used for the successor of the Hyperion-I scanner, but instead of using analog SiPMs, the Hyperion-II^D scanner employs digital SiPMs (dSiPM) which digitize the breakdown of each SPAD individually, no further digitization is needed [25]. Therefore, the complete digitization is performed inside the MRI system and digital information is sent via an optical ethernet link to a data acquisition system used for coincidence processing. First results on the PET/MR interference of a single PET module of the upgraded platform using dSiPMs and a preclinical scintillator configuration were presented in [26].

The dSiPM is less prone to variations in the bias voltage due to temperature or voltage fluctuations. In 2009, Philips Digital Photon Counting (PDPC) presented the first dSiPM [27]–[29]. The Hyperion-II^D scanner employs PDPC digital photomultiplier DPC 3200-22 (DPC) sensors.

In this work, we use the Hyperion-II^D platform equipped with a scintillator configuration closer to a clinical application using a one-to-one coupling of crystals and read-out channels. This arrangement results in a better timing performance compared to using a light-sharing technique and allows a higher sensitivity for investigations of the ToF performance of the platform and its behavior during simultaneous MR operation.

We present for the first time two modules fully equipped with clinical scintillators and a readout based on PDPC's DPCs which are ToF capable and operated in a 3-T MRI system. We focus on gradient stress tests as used in [26] which show the strongest influence on the PET performance [14] [30].

II. MATERIALS

The system employs detector stacks [31] equipped with a pixelated LYSO crystal scintillator array with 8×8 crystals, 10 mm height and a pitch of 4 mm. Our group developed an MR-compatible sensor tile which is used to read out the crystal scintillator and employs PDPC digital photomultiplier DPC 3200-22 sensors [28], [29]. The sensor tile is 32.6×32.6 mm^2 in size and made up of 16 individual DPCs. Each DPC comprises 2×2 pixels (also referred to as read-out channel) consisting of 3200 digital SPADs which can be disabled individually. This leads to a one-to-one coupling of each crystal to a single read-out channel. The sensor tile is read out and controlled via an interface board which houses an FPGA (Xilinx Spartan-6) [32].
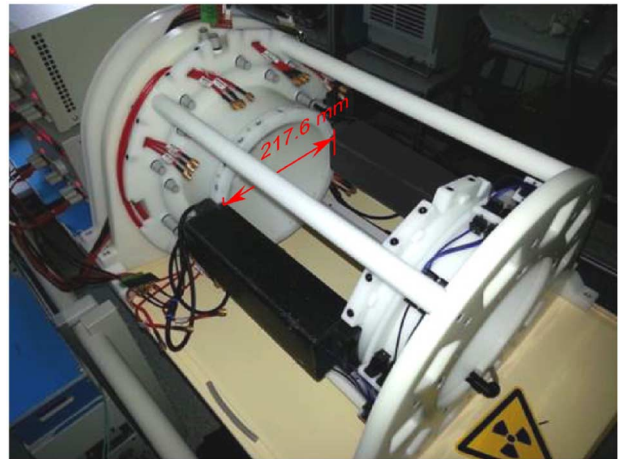

Fig. 1. Two modules are mounted on a gantry (gantry position) in horizontally opposite positions with a distance of 217.6 mm measured between crystals. In a second arrangement, they are placed in maximum distance inside the MR bore of approximately 410 mm (maximum distance position).

Up to six sensor stacks can be mounted onto a singles-detection module (SDM) in a 2×3 arrangement [33]. An FPGA (Xilinx Virtex-5) on the main module PCB handles the communication with the detector stacks [32]. Each SDM is connected to a data acquisition and processing server (DAPS) [34] via plastic optical fibers (POF). The DAPS is controlled via a control PC and routes the status and command communication between the latter and the SDMs. Hit data is either processed for coincidences in real time or stored for offline analysis on the DAPS. An additional POF per SDM is connected to a central synchronization and trigger unit which is used to generate the system-wide clock.

From a switched mode power supply, three galvanically isolated power lines provide two low operating and the supply voltage for the bias voltage for the DPCs to every SDM. The SDMs employ a carbon fiber housing for radio frequency and light shielding [35]. The insert is cooled using a liquid cooling system and is additionally flooded with dry air allowing for a stable temperature control and preventing condensation.

In this work, we use two fully equipped SDMs horizontally facing each other at two different distance configurations: first, the so-called *gantry position* and second, a *maximum distance position*. At the gantry position, the distance between the modules (crystal-to-crystal) is 217.6 mm. This is the default distance when using the Hyperion-II^D platform (Fig. 1). At the maximum distance position, we move the SDMs inside the MR bore as far as possible to the inner wall of the bore (the approximate distance is 410 mm).

III. METHODS

The DPCs are operated at a cooling temperature of $0°C$ leading to $5-10°C$ measured on the sensor tile under operation.

We measure the breakdown voltage of each sensor tile defined as the bias voltage at which the SPADs start to breakdown. The resulting breakdown voltage is stored and an additional overvoltage (V_{ov}) is applied to define the final bias voltage for operation. Conservatively, we choose to disable 20% of the worst cells and use an overvoltage of $V_{ov} = 2.0$ V and 2.5 V.

To obtain the best time stamp performance, we use the trigger scheme 1 (first photon trigger) and a high validation threshold of 52 photons (validation scheme in hexadecimal notation: 0x00:OR) [36], [37]. We do not employ the neighbor triggering capabilities of the DPCs [38].

Pixel photon values are corrected for saturation and DPC hits are temporally clustered using a cluster window of 40 ns.

Exploiting the one-to-one coupling, the crystal bin can and is identified from the highest photon count of the cluster. The energy is calculated using the four pixels of the DPC housing the main pixel.

A narrow energy window of 511 ± 50 keV is used, and to further improve the time stamp performance, we reject detector scatter events by requesting a minimal light fraction of the main pixel of more than 65% of the photon sum of all DPCs of a cluster.

The timing difference for each measured pair of scintillator crystals in the system is histogrammed. A single delay value per scintillator crystal is fitted to all measured difference values using least squares fitting.

By using a ^{22}Na point source in the isocenter of the modules, the CRT of the scanner is evaluated during and in the absence of MR sequences.

As described in [26], several stress tests with switching gradients are performed. We use demanding sequences with a high gradient strength and duty cycle based on a normal EPI sequence (EPI factor: 49, gradient strength: 30 mT/m, slew rate: 192.3 mT/m/ms, TE/TR: 12/25 ms and switching duty cycle: 67% with gradients in x-, y- and z-direction).

For each gradient test we take PET data for approximately 3 min and apply the MR sequence in a time window of 1 min in the middle of the measurement window. The energy spectrum and timing difference histogram of the two SDMs is determined in 40 s time windows before, during and after the MR sequence. The energy resolution is determined by iteratively fitting a Gaussian to the energy spectrum in the range of -0.5 to 1 FWHM around the photo peak. In the same way we iteratively fit a Gaussian to the timing difference histogram to match a range of -0.5 to 0.5 FWHM around the peak. The degradation of the energy resolution and CRT during the MR sequence to the values before and after the sequence are computed as relative changes.

We showed in [26] that we could not measure a loss of sensor data due to gradient switching before singles processing. A loss of counts is caused by the degradation of the energy resolution. The loss of counts depends on the selected energy window in conjunction with the induced degradation. We showed that a large window leads to no loss of counts. These findings are consistent with the measurements in this work. Therefore, we do not investigate count rate losses in detail in this work as the underlying platform is the same. We will state the loss of coincident prompts for the most aggressive setting for the given energy window.

IV. RESULTS

Inside the B_0 field when no further MR operation is performed the energy resolution is determined to be 11.5% (FWHM) and the CRT 250 ps (FWHM) for an overvoltage of

$V_{ov} = 2.0$ V. Applying an overvoltage of $V_{ov} = 2.5$ V yields an energy resolution of 11.2% (FWHM) and a CRT of 240 ps (FWHM).

The results of the gradient influence are listed in Table I. Histograms for time differences between the two SDMs as a function of time are shown in Fig. 2 and Fig. 3. The energy histogram for the measurement with the SDMs mounted on the gantry (gantry postition) and using an overvoltage of $V_{ov} = 2.5$ V is shown in Fig. 4. The x-gradient does not show any influence on the energy or timing performance for any of the positions and applied overvoltages. At the gantry position using an overvoltage of $V_{ov} = 2.0$ V during the y- and z-gradient sequences, the energy resolution is degraded by 0.7% and 4.1%, the CRT by 20% and 25%, respectively. At an overvoltage of $V_{ov} = 2.5$ V the z-gradient sequence degrades the energy resolution by 3.3% and the CRT by 30% to 314 ps. When the SDMs are placed closest to the gradient coils at the maximum distance inside the MR bore (maximum distance position), the energy resolution is degraded by 0.4% and 9.2% (Fig. 4), the CRT by 26% to 302 ps and 52% to 365 ps when applying an overvoltage of $V_{ov} = 2.5$ V for y- and z-gradient sequences, respectively.

For the most aggressive scenario (maximum distance position, z-gradient) we observe prompt losses of $3 - 4\%$ for the selected energy window. No loss of unfiltered singles was found.

V. DISCUSSION AND CONCLUSION

Energy resolution and CRT degradations can be observed during demanding gradient sequences. The x-gradient does not show any measurable influence on the performance whereas the y-gradient shows a clear influence. Z-gradient switching shows the largest influence on the performance of the two modules. This can be explained by the orientation of the SDMs inside the MR bore and the resulting magnetic flux going through the main PCB.

As previously described in [26], we observe a ripple on the bias voltage during gradient switching. We assume that this ripple is responsible for the observed energy degradation during gradient switching, as the applied bias voltage directly influences the photon detection efficiency. A photon detection efficiency variation introduces a variation in measured energy values, which, in turn, leads to a decrease in energy resolution.

No loss of sensor data can be measured. Unfiltered single rates do not show any influence. Count rate losses of prompts are caused by degradation of the energy resolution (Fig. 4) in conjunction with the narrow energy window [26]. This behavior has been observed for an APD based system as well [30].

Although the DPC-based PET detector operates stable under MR conditions, we show that its timing and energy performance is sensitive to gradient switching. So far, we could not find any evidence that the performance degradations can be ascribed to the DPC itself. The MR sequence used is optimized purely for continuous gradient switching with maximum possible slew rates and is not useful for diagnostic MRI. Our measurements represent an temporal averaging of distortions for this worst-case scenario. We expect that the degradation for common MR sequences is far less and probably negligible for most standard imaging protocols. The highest duty cycle
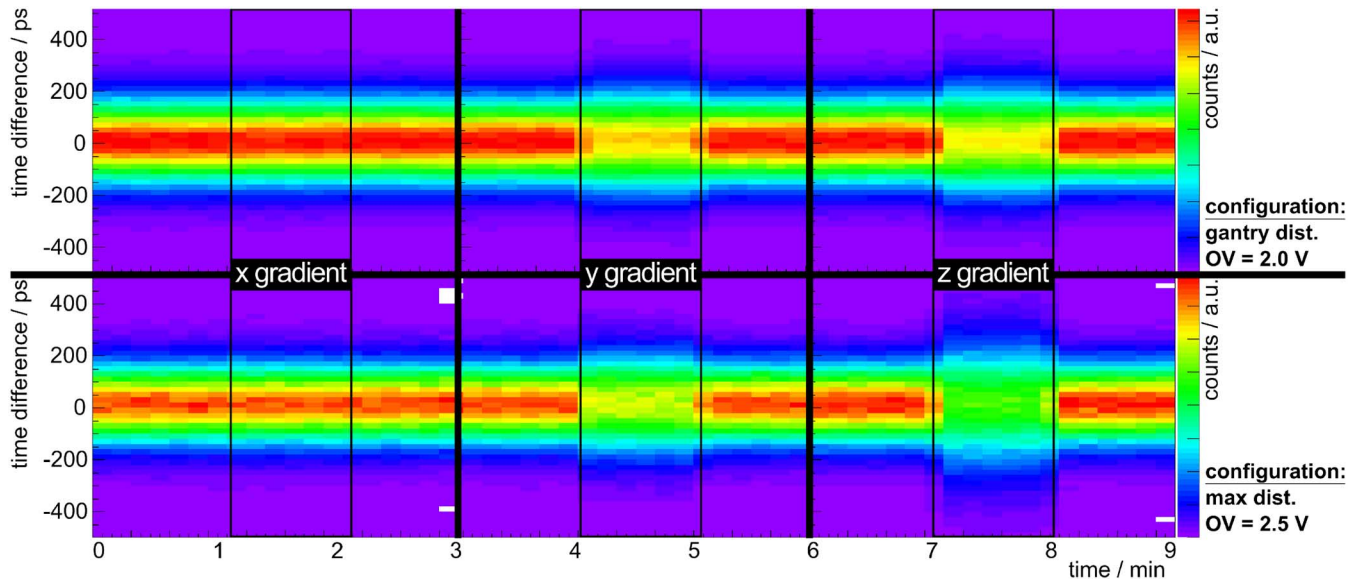
Fig. 2. The time difference histogram of the two modules as a function of time for measurements of 3 min length per gradient with a gradient sequence in the middle of the measurement of 1 min. The upper histograms show measurements using the gantry position and an overvoltage of $V_{ov} = 2.0$ V. The lower histograms are obtained using the maximum distance of the SDMs (maximum distance position) and an overvoltage of $V_{ov} = 2.5$ V. The columns from left to right show measurements with a high demanding gradient switching sequence in x, y and z direction. At the beginning and the end of the MR sequence, binning artifacts might be observed. White bins have no entries.
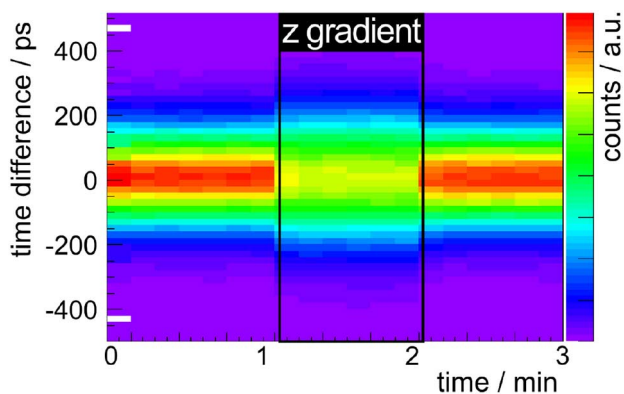

Fig. 3. The time difference histogram of two modules in gantry position as a function of time for a measurement of 3 min length with a z-gradient sequence in the middle of the measurement of 1 min. An overvoltage of $V_{ov} = 2.5$ V is applied. At the beginning and the end of the MR sequence, binning artifacts might be observed. White bins have no entries.
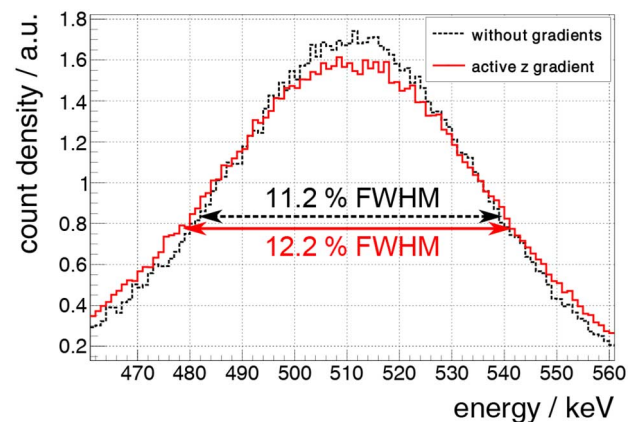

Fig. 4. The energy histogram around the photo peak is shown for two modules at closest position to the gradient system inside the MRI system (maximum distance position) using an overvoltage of $V_{ov} = 2.5$ V. In dashed black the energy histogram for a measurement without gradient activity is shown. In continuous red the energy histogram for the MR sequence with a maximum z-gradient activity is shown. The energy resolution is degraded by 9.2%.

for imaging sequences shown in [24] are smaller than 20% which leads to a smaller fraction of PET data influenced due to gradient switching compared to the sequence shown in this paper. Nevertheless, for future system designs – especially if the detector is placed closer to the gradient system and therefore is exposed to higher magnetic fluxes – these effects should be considered to enable simultaneous PET/MR without performance tradeoffs between both modalities.

The underlying Hyperion-II^D platform proofs to deliver good timing performance and energy resolution both during MR silence and during highly demanding MR gradient sequences. We successfully operated DPC-based fully digital PET modules with a clinical scintillator configuration in a 3-T MRI system achieving a CRT of 240 ps and an energy resolution of 11.2%

which is, to our knowledge, the best performance shown for a PET/MR system so far.

VI. OUTLOOK

A detailed investigation of the vulnerability to heavy gradient switching is currently ongoing. Flexible MR sequence programming has been developed which allows to freely program slew rates and duty cycles. This may allow a deeper understanding of the interference between the MRI system and the PET insert. The SDM design is reviewed for possible improvements concerning MR compatibility.

TABLE I

DETERMINED ENERGY AND TIMING RESOLUTION (CRT) FOR THE DIFFERENT MEASUREMENTS (POSITIONS = GANTRYPOSITION, MAXMAXIMUM DISTANCE POSITION, OVERVOLTAGES) UNDER DIFFERENT GRADIENT CONDITIONS (NO GRADIENTS, MAXIMUM x-GRADIENT, MAXIMUM y-GRADIENT AND MAXIMUM z-GRADIENT). IN ADDITION TO THE RESOLUTION VALUES, THE DEGRADATION WITH REFERENCE TO THE MEASUREMENT WITHOUT MR ACTIVITY IS CALCULATED. FOR ALL EXPERIMENTS, THE TRIGGER SCHEME 1 WAS USED

Position	OV / V	Condition	Energy resolution FWHM / %	Energy resolution Degradation	CRT FWHM / ps	CRT Degradation
Gantry	2.0	no grad.	11.5	no significant degradation	250	no significant degradation
		max. X	11.5		250	
		no grad.	11.5	0.7 %	251	20 %
		max. Y	11.6		303	
		no grad.	11.5	4.1 %	253	25 %
		max. Z	11.9		317	
	2.5	no grad.	11.2	3.3 %	241	30 %
		max. Z	11.6		314	
max. distance	2.5	no grad.	11.2	no significant degradation	240	no significant degradation
		max. X	11.1		240	
		no grad.	11.2	0.4 %	240	26 %
		max. Y	11.2		302	
		no grad.	11.2	9.2 %	241	52 %
		max. Z	12.2		365	

A full PET ring using 10 SDMs using the scintillator configuration described in this work is intensely studied for MR compatibility. This will allow an evaluation for a clinical scintillator and read-out configuration using DPCs on a full system level.

REFERENCES

[1] D. W. Townsend, "Combined positron emission tomography-computed tomography: The historical perspective," *Semin. Ultrasound, CT MRI*, vol. 29, no. 4, pp. 232–235, 2008, doi:10.1053/j.sult.2008.05.006, PET/CT.

[2] C. Buchbender, T. A. Heusner, T. C. Lauenstein, A. Bockisch, and G. Antoch, "Oncologic PET/MRI, part 1: Tumors of the brain, head and neck, chest, abdomen, and pelvis," *J. Nucl. Med.*, vol. 53, no. 6, pp. 928–938, Jun. 2012, doi:10.2967/jnumed.112.105338.

[3] C. Buchbender, T. A. Heusner, T. C. Lauenstein, A. Bockisch, and G. Antoch, "Oncologic PET/MRI, part 2: Bone tumors, soft-tissue tumors, melanoma, and lymphoma," *J. Nucl. Med.*, vol. 53, no. 8, pp. 1244–1252, Aug. 2012, doi:10.2967/jnumed.112.109306.

[4] G. K. von Schulthess and H.-P. W. Schlemmer, "A look ahead: PET/MR versus PET/CT," *Eur. J. Nucl. Med. Mol. Imag.*, vol. 36, no. 1, pp. 3–9, 2009, doi:10.1007/s00259-008-0940-9.

[5] H. Jadvar and P. M. Colletti, "Competitive advantage of PET/MRI," *Eur. J. Radiol.*, vol. 83, no. 1, pp. 84–94, 2014, doi:10.1016/j.ejrad.2013.05.028.

[6] A. Drzezga, M. Souvatzoglou, M. Eiber, A. J. Beer, S. Fürst, A. Martinez-Möller, S. G. Nekolla, S. Ziegler, C. Ganter, and E. J. Rummeny *et al.*, "First clinical experience with integrated whole-body pet/mr: Comparison to pet/ct in patients with oncologic diagnoses," *J. Nucl. Med.*, vol. 53, no. 6, pp. 845–855, 2012, doi:10.2967/jnumed.111.098608.

[7] M. S. Judenhofer and S. R. Cherry, "Applications for preclinical PET/MRI," in *Seminars in Nuclear Medicine*. New York, NY, USA: Elsevier, 2013, vol. 43, pp. 19–29, doi:10.1053/j.semnuclmed.2012.08.004.

[8] Y. Shao, S. R. Cherry, K. Farahani, K. Meadors, S. Siegel, R. W. Silverman, and P. K. Marsden, "Simultaneous PET and MR imaging," *Phys. Med. Biol.*, vol. 42, no. 10, 1965, 1997, doi:10.1088/0031-9155/42/10/010.

[9] Y. Shao, S. Cherry, K. Farahani, R. Slates, R. Silverman, K. Meadors, A. Bowery, S. Siegel, P. Marsden, and P. Garlick, "Development of a pet detector system compatible with MRI/NMR systems," *IEEE Trans. Nucl. Sci.*, vol. 44, no. 3, pp. 1167–1171, Jun. 1997.

[10] P. B. Garlick, P. K. Marsden, A. C. Cave, H. G. Parkes, R. Slates, Y. Shao, R. W. Silverman, and S. R. Cherry, "PET and NMR dual acquisition (PANDA): Applications to isolated, perfused rat hearts," *NMR Biomed.*, vol. 10, no. 3, pp. 138–142, 1997, doi:10.1002/(SICI)1099-1492(199705)10:3 ⟨138 :: AID − NBM474⟩3.0.CO; 2 − H.

[11] B. J. Pichler, M. S. Judenhofer, C. Catana, J. H. Walton, M. Kneilling, R. E. Nutt, S. B. Siegel, C. D. Claussen, and S. R. Cherry, "Performance test of an LSO-APD detector in a 7-T MRI scanner for simultaneous PET/MRI," *J. Nucl. Med.*, vol. 47, no. 4, pp. 639–647, 2006.

[12] M. S. Judenhofer, H. F. Wehrl, D. F. Newport, C. Catana, S. B. Siegel, M. Becker, A. Thielscher, M. Kneilling, M. P. Lichy, and M. Eichner *et al.*, "Simultaneous PET-MRI: A new approach for functional and morphological imaging," *Nature Med.*, vol. 14, no. 4, pp. 459–465, 2008, doi:10.1038/nm1700.

[13] C. Catana, Y. Wu, M. S. Judenhofer, J. Qi, B. J. Pichler, and S. R. Cherry, "Simultaneous acquisition of multislice PET and MR images: Initial results with a MR-compatible PET scanner," *J. Nucl. Med.*, vol. 47, no. 12, pp. 1968–1976, 2006.

[14] C. Catana, D. Procissi, Y. Wu, M. S. Judenhofer, J. Qi, B. J. Pichler, R. E. Jacobs, and S. R. Cherry, "Simultaneous in vivo positron emission tomography and magnetic resonance imaging," *Proc. Nat. Acad. Sci.*, vol. 105, no. 10, pp. 3705–3710, 2008, doi:10.1073/pnas.0711622105.

[15] B. J. Pichler, H. F. Wehrl, and M. S. Judenhofer, "Latest advances in molecular imaging instrumentation," *J. Nucl. Med.*, vol. 49, pp. 5S–23S, 2008, doi:10.2967/jnumed.108.045880, Suppl 2.

[16] H. Zaidi and A. Del Guerra, "An outlook on future design of hybrid PET/MRI systems," *Med. Phys.*, vol. 38, no. 10, pp. 5667–5689, 2011, doi:10.1118/1.3633909.

[17] J. A. Disselhorst, I. Bezrukov, A. Kolb, C. Parl, and B. J. Pichler, "Principles of PET/MR imaging," *J. Nucl. Med.*, vol. 55, pp. 2S–10S, 2014, doi:10.2967/jnumed.113.129098, Suppl 2.

[18] S. J. Hong, I. C. Song, M. Ito, S. I. Kwon, G. S. Lee, K.-S. Sim, K.-S. Park, J. T. Rhee, and J. S. Lee, "An investigation into the use of geiger-mode solid-state photomultipliers for simultaneous PET and MRI acquisition," *IEEE Trans. Nucl. Sci.*, vol. 55, no. 3, pp. 882–888, Jun. 2008.

[19] J. Kang, Y. Choi, K. J. Hong, J. H. Jung, W. Hu, Y. S. Huh, H. Lim, and B.-T. Kim, "A feasibility study of photosensor charge signal transmission to preamplifier using long cable for development of hybrid PET-MRI," *Med. Phys.*, vol. 37, no. 11, pp. 5655–5664, 2010, doi:10.1118/1.3495683.

[20] J. Kang, Y. Choi, K. J. Hong, W. Hu, J. H. Jung, Y. Huh, and B.-T. Kim, "A small animal PET based on GAPDs and charge signal transmission approach for hybrid PET-MR imaging," *J. Instrum.*, vol. 6, no. 08, p. P08012, 2011, doi:10.1088/1748-0221/6/08/P08012.

[21] S. Yamamoto, T. Watabe, H. Watabe, M. Aoki, E. Sugiyama, M. Imaizumi, Y. Kanai, E. Shimosegawa, and J. Hatazawa, "Simultaneous imaging using Si-PM-based PET and MRI for development of an integrated PET/MRI system," *Phys. Med. Biol.*, vol. 57, no. 2, p. N1, 2012, doi:10.1088/0031-9155/57/2/N1.

[22] H. S. Yoon, G. B. Ko, S. I. Kwon, C. M. Lee, M. Ito, I. C. Song, D. S. Lee, S. J. Hong, and J. S. Lee, "Initial results of simultaneous PET/MRI experiments with an MRI-compatible silicon photomultiplier PET scanner," *J. Nucl. Med.*, vol. 53, no. 4, pp. 608–614, 2012, doi:10.2967/jnumed.111.097501.

[23] V. Schulz, T. Solf, B. Weissler, P. Gebhardt, P. Fischer, M. Ritzert, V. Mlotok, C. Piemonte, N. Zorzi, M. Melchiorri, S. Vandenberghe, V. Keereman, T. Schaeffter, and P. Marsden, "A preclinical PET/MR insert for a human 3T MR scanner," in *Proc. IEEE Nuclear Science Symp. Conf. Rec.*, Oct. 2009, pp. 2577–2579, doi:10.1109/NSSMIC.2009.5402018.

[24] B. Weissler, P. Gebhardt, C. Lerche, J. Wehner, T. Solf, B. Goldschmidt, J. E. Mackewn, P. Marsden, F. Kiessling, M. Perkuhn, D. Heberling, and V. Schulz, "MR compatibility aspects of a silicon photomultiplier-based PET/RF insert with integrated digitisation," *Phys. Med. Biol.*, vol. 59, no. 17, p. 5119, 2014, doi:10.1088/0031-9155/59/17/5119.

[25] B. Weissler, P. Gebhardt, P. Dueppenbecker, B. Goldschmidt, A. Salomon, D. Schug, J. Wehner, C. Lerche, D. Wirtz, W. Renz, K. Schumacher, B. Zwaans, P. Marsden, F. Kiessling, and V. Schulz, "Design concept of world's first preclinical PET/MR insert with fully digital silicon photomultiplier technology," in *Proc. IEEE Nuclear Science Symp. and Medical Imaging Conf.*, Oct. 2012, p. 2113, doi:10.1109/NSSMIC.2012.6551484.

[26] J. Wehner, B. Weissler, P. Dueppenbecker, P. Gebhardt, D. Schug, W. Ruetten, F. Kiessling, and V. Schulz, "PET/MRI insert using digital SiPMs: Investigation of MR-compatibility," *Nucl. Instrum. Methods Phys. Res. A*, vol. 734, pp. 116–121, 2014, doi:10.1016/j.nima.2013.08.077.

[27] T. Frach, G. Prescher, C. Degenhardt, R. de Gruyter, A. Schmitz, and R. Ballizany, "The digital silicon photomultiplier–principle of operation and intrinsic detector performance," in *Proc. IEEE Nuclear Science Symp. Conf. Rec.*, Nov. 2009, pp. 1959–1965, doi:10.1109/NSSMIC.2009.5402143.

[28] T. Frach, G. Prescher, C. Degenhardt, and B. Zwaans, "The digital silicon photomultiplier–system architecture and performance evaluation," in *Proc. IEEE Nuclear Science Symp. Conf. Rec.*, Nov. 2010, pp. 1722–1727, doi:10.1109/NSSMIC.2010.5874069.

[29] C. Degenhardt, P. Rodrigues, A. Trindade, B. Zwaans, O. Mülhens, R. Dorscheid, A. Thon, A. Salomon, and T. Frach, "Performance evaluation of a prototype positron emission tomography scanner using digital photon counters (DPC)," in *Proc. IEEE Nuclear Science Symp. and Medical Imaging Conf.*, Oct. 2012, p. 2820, doi:10.1109/NSSMIC.2012.6551643.

[30] C. Weirich, D. Brenner, J. Scheins, E. Besancon, L. Tellmann, H. Herzog, and N. Shah, "Analysis and correction of count rate reduction during simultaneous MR-PET measurements with the BrainPET scanner," *IEEE Trans. Med. Imag.*, vol. 31, no. 7, pp. 1372–1380, Jul. 2012.

[31] P. Dueppenbecker, B. Weissler, P. Gebhardt, D. Schug, J. Wehner, P. Marsden, and V. Schulz, "Development of an MRI compatible digital SiPM based PET detector stack for simultaneous preclinical PET/MRI," in *Proc. IEEE Nuclear Science Symp. and Medical Imaging Conf.*, Oct. 2012, pp. 3481–3483, doi:10.1109/NSSMIC.2012.6551794.

[32] P. Gebhardt, B. Weissler, M. Zinke, F. Kiessling, P. Marsden, and V. Schulz, "FPGA-based singles and coincidences processing pipeline for integrated digital PET/MR detectors," in *Proc. IEEE Nuclear Science Symp. and Medical Imaging Conf.*, Oct. 2012, pp. 2479–2482, doi:10.1109/NSSMIC.2012.6551565.

[33] B. Weissler, P. Gebhardt, M. Zinke, F. Kiessling, and V. Schulz, "An MR-compatible singles detection and processing unit for simultaneous preclinical PET/MR," in *Proc. IEEE Nuclear Science Symp. and Medical Imaging Conf.*, Oct. 2012, pp. 2759–2761, doi:10.1109/NSSMIC.2012.6551628.

[34] B. Goldschmidt, C. W. Lerche, T. Solf, A. Salomon, F. Kiessling, and V. Schulz, "Towards software-based real-time singles and coincidence processing of digital PET detector raw data," *IEEE Trans. Nucl. Sci.*, vol. 60, no. 3, pp. 1550–1559, Jun. 2013.

[35] P. Dueppenbecker, J. Wehner, W. Renz, S. Lodomez, D. Truhn, P. Marsden, and V. Schulz, "Gradient transparent RF housing for simultaneous PET/MRI using carbon fiber composites," in *Proc. IEEE Nuclear Science Symp. and Medical Imaging Conf.*, Oct. 2012, pp. 3478–3480, doi:10.1109/NSSMIC.2012.6551793.

[36] "Philips digital photon couting," PDPC-TEK User Manual v0.21, 2014.

[37] V. Tabacchini, V. Westerwoudt, G. Borghi, S. Seifert, and D. Schaart, "Probabilities of triggering and validation in a digital silicon photomultiplier," *J. Instrum.*, vol. 9, no. 06, p. P06016, 2014, doi:10.1088/1748-0221/9/06/P06016.

[38] D. Schug, P. M. Dueppenbecker, P. Gebhardt, B. Weissler, B. Zwaans, F. Kiessling, and V. Schulz, "First evaluations of the neighbor logic of the digital SiPM tile," in *Proc. IEEE Nuclear Science Symp. and Medical Imaging Conf.*, Oct. 2012, p. 2817, doi:10.1109/NSSMIC.2012.6551642.